

1 **Macrovesicular steatosis in nonalcoholic fatty liver disease is a consequence of**
2 **purine nucleotide cycle driven fumarate accumulation**

3

4 **Authors:**

5 Matthew C. Sinton¹, Baltasar Lucendo Villarin², Jose Meseguer Ripolles², Sara Wernig-
6 Zorc³, John P. Thomson⁴, Paul D. Walker⁵, Alpesh Thakker⁵, Gareth G. Lavery⁵, Christian
7 Ludwig⁵, Daniel A. Tennant⁵, David C. Hay², Amanda J. Drake^{1*}

8

9 **Author Affiliations:**

10 1. University/BHF Centre for Cardiovascular Science, The Queen's Medical Research
11 Institute, Edinburgh BioQuarter, 47 Little France Crescent, Edinburgh EH16 4TJ

12 2. Centre for Regenerative Medicine, Institute for Regeneration and Repair, Edinburgh
13 BioQuarter, 5 Little France Crescent, Edinburgh, EH16 4UU

14 3. Department of Biochemistry, University of Regensburg, Universitätsstraße 31, 93053
15 Regensburg, Germany

16 4. Human Genetics Unit, MRC Institute for Genetics and Molecular Medicine, University of
17 Edinburgh, Crewe Road South, Edinburgh, EH4, 2XU

18 5. Institute of Metabolism and Systems Research, IBR Tower, College of Medical and Dental
19 Sciences, Edgbaston, University of Birmingham, Birmingham, B15 2TT

20

21

22

* **Corresponding Author:**

Amanda J. Drake: University/BHF Centre for Cardiovascular Science, Queen's Medical Research Institute, Edinburgh BioQuarter, 47 Little France Crescent, Edinburgh EH16 4TJ.
mandy.drake@ed.ac.uk

23 **Summary**

24 Nonalcoholic fatty liver disease (NAFLD) affects ~88% of obese individuals and is
25 characterised by hepatic lipid accumulation. Mitochondrial metabolic dysfunction is a feature
26 of NAFLD. We used a human pluripotent stem cell-based system to determine how
27 mitochondrial dysfunction is linked to hepatic lipid accumulation. We induced lipid
28 accumulation in hepatocyte-like cells (HLCs) using lactate, pyruvate and octanoate (LPO).
29 Transcriptomic analysis revealed perturbation of mitochondrial respiratory pathways in LPO
30 exposed cells. Using ¹³C isotopic tracing, we identified truncation of the TCA cycle in
31 steatotic HLCs. We show that increased purine nucleotide cycle (PNC) activity fuels
32 fumarate accumulation and drives lipid accumulation in steatotic cells. These findings
33 provide new insights into the pathogenesis of hepatic steatosis and may lead to an improved
34 understanding of the metabolic and transcriptional rewiring associated with NAFLD.

35

36 **Keywords:**

37 Nonalcoholic fatty liver disease, steatosis, TCA cycle, mitochondria, purine nucleotide cycle,
38 fumarate, succinate

39

40

41

42

43

44

45

46

47

48

49

50

51 **Introduction**

52 Nonalcoholic fatty liver disease (NAFLD) is the most common form of hepatic disease and is
53 strongly associated with obesity and the development of type 2 diabetes (WHO, 2006). In
54 the earliest stage of NAFLD, triglyceride (TG) accumulation in hepatocytes leads to the
55 development of hepatic steatosis (Valenti et al., 2016). This is characterised by the
56 development of macrovesicular steatosis, whereby TGs are stored in large lipid droplets
57 (Wang and Yu, 2016). Whilst steatosis is largely benign, it can progress to nonalcoholic
58 steatohepatitis (NASH), which, in turn, increases the risk of developing cirrhosis and
59 hepatocellular carcinoma (Asrih and Jornayvaz, 2015). However, the mechanism(s)
60 underlying this progression have yet to be determined. At present, there are no specific
61 therapeutics available to reverse or treat NAFLD, and the only effective intervention is
62 through the reduction of obesity following bariatric surgery (Laursen et al., 2019).

63

64 NAFLD has been linked to impaired mitochondrial respiration, with previous findings
65 revealing altered electron transport chain (ETC) activity associated with steatosis (Koliaki et
66 al., 2015; Sinton et al., 2020). Rodent studies suggest that steatosis is preceded by
67 mitochondrial dysfunction, indicating that NAFLD and its progression may, in part, be a
68 consequence of impaired mitochondrial respiration (Rector et al., 2010). Further, hepatic
69 steatosis in mice is accompanied by increased tricarboxylic acid (TCA) cycle activity
70 (Satapati et al., 2012). Human studies also suggest that NAFLD is associated with increased
71 TCA cycle activity, with increased movement of substrates into and out of the TCA cycle
72 alongside increased rates of gluconeogenesis and lipolysis (Sunny et al., 2011). However,
73 whilst informative, these studies were indirect and used measurements of plasma
74 metabolites to infer hepatic metabolic flux, rather than directly measuring levels within the
75 liver. Examination of TCA cycle function in mouse models of NAFLD identified increased
76 hepatic TCA cycle flux (Satapati et al., 2015). Limiting pyruvate transport into the
77 mitochondria reduces mitochondrial flux and limits the development of NASH-associated
78 inflammation (Rauckhorst et al., 2017). However, metabolic flux analysis in whole tissue is

79 confounded by the presence of heterogeneous cell populations, each of which may have a
80 different metabolic phenotype (Antoniewicz, 2018). Studies in primary rat hepatocytes show
81 that modulation of TCA cycle anaplerosis fuels oxidative stress and enhances development
82 of a NASH phenotype (Egnatchik et al., 2019). One limitation of primary cells is that they
83 rapidly lose their phenotype and display altered transcriptional signatures on purification
84 (Godoy et al., 2016; Knobeloch et al., 2012). In these studies, we employed a renewable
85 form of human liver tissue (Wang et al., 2019b). To our knowledge, high-resolution
86 metabolomic analyses have not been performed in a renewable human system, providing
87 the field with new insight into human liver disease.

88

89 The TCA cycle metabolites alpha-ketoglutarate (α KG), succinate and fumarate are allosteric
90 regulators of the α KG-dependent dioxygenase family of enzymes; their activity is promoted
91 by α KG and inhibited by succinate and fumarate (Hausinger, 2004; Roach et al., 1995; Xiao
92 et al., 2012). The Fe(II)/O₂-dependent enzymes include the Jumonji domain-containing
93 histone demethylases (JHDMs), prolyl-4-hydroxylases, and the ten-eleven translocation
94 (TET) dioxygenases (Laukka et al., 2016; McDonough et al., 2010). The JHDMs and TET
95 enzymes can regulate the epigenome through modulation of histone and DNA methylation,
96 respectively, with the latter oxidising 5-methylcytosine to 5-hydroxymethylcytosine (5hmC)
97 (Pollard et al., 2008; Tahiliani et al., 2009). In human cancers, mutations in succinate
98 dehydrogenase and fumarate hydratase result in the accumulation of succinate and
99 fumarate, which inhibit JHDM and TET dioxygenase activity and may contribute to
100 tumourigenesis (Xiao et al., 2012). Dysregulation of the α KG-dependent dioxygenase
101 enzymes may also be important in the pathogenesis of liver disease; we have previously
102 identified alterations in 5hmC at specific loci in murine and human models of NAFLD,
103 suggesting a role for the TET enzymes, which oxidise 5-methylcytosine (5mC) to 5-
104 hydroxymethylcytosine (5hmC) (Lyall et al., 2020). Studies in mouse models of
105 hepatocellular carcinoma suggest that the TET enzymes may also contribute to the

106 progression of liver cancer, through perturbation of normal DNA demethylation events at
107 promoters (Thomson et al., 2016).

108

109 In this study, we aimed to understand the impact of lipid accumulation on TCA cycle activity
110 and whether this influences TET enzyme activity. We performed these studies in a reliable
111 model of NAFLD (Lyall et al., 2018) which enables us to repeatedly study hepatocyte biology
112 in isolation, avoiding the confounding effects of tissue disaggregation, bulk tissue analysis or
113 inferred measurement.

114

115 **Results**

116 **LPO treatment induces intracellular lipid accumulation and transcriptomic alterations**
117 **in key mitochondrial respiratory pathways**

118 HLC exposure to LPO resulted in macrovesicular steatosis (Fig. 1A), as previously reported
119 (Sinton et al., 2020). This was associated with widespread transcriptomic changes (Fig. 1B).
120 Differential gene expression analysis identified 853 downregulated and 826 upregulated
121 genes (\log_2 fold change cut-off >1.5) in LPO exposed cells compared with control. A
122 selection of candidate genes was validated by RT-qPCR (Fig. S2). From the RNA-seq
123 analysis, we observed altered expression of a number of genes previously described as
124 having function roles in the progression of NAFLD, including PLIN2, PPARGC1A, CYP7A1,
125 and HMGCS2 (Fig. 1C). Mapping genes with a \log_2 fold change >1.5 to the KEGG pathway
126 database identified a number of enriched pathways (Fig. 1D & 1E), including those related to
127 steroid hormone biosynthesis and ascorbate and aldarate metabolism, containing 18 and 7
128 genes respectively (Table S1). There was extensive downregulation of the histone structural
129 units H1, H2A/B, H3 and H4 and UDP-glucuronosyltransferases, which were enriched in
130 multiple pathways. Specifically comparing transcriptomic data with the KEGG terms 'TCA
131 Cycle' and 'Oxidative Phosphorylation' revealed extensive gene expression changes within
132 these pathways (Fig. 1F & 1G) including in the majority of genes encoding enzymes that
133 catalyse metabolite interconversion (Table S2). Analysis of the Oxidative Phosphorylation
134 pathway revealed an overall downregulation of transcription of genes encoding components
135 of respiratory complexes I (ND1, ND2, ND4L, NDUFS2, NDUFV1, NDUFA10, NDUFB2
136 NDUFA2, NDUFB10) and IV (COX1, COX4I1, COX8A, COX6B1), as well as ATP synthase
137 (ATP6V1A, ATP5MF, ATP6V0D1, ATP6V1E1, ATP6, APT5MC2, ATP5MC1) (Table S3).

138

139

140

141

142 **Induction of a NAFLD-like phenotype in HLCs is associated with increased pyruvate**
143 **carboxylase activity**

144 To investigate TCA cycle dynamics, lactate in the LPO cocktail was replaced with $^{13}\text{C}_3$ -
145 lactate. Lactate can enter the TCA cycle *via* mitochondrial pyruvate metabolism, through
146 either pyruvate carboxylase (PC) or pyruvate dehydrogenase (PDH). Alternatively, pyruvate
147 can be transported into the cytosol and used in gluconeogenesis (Fig. 2A). LPO exposure
148 was associated with increases in steady state levels of pyruvate, aspartate and citrate, but
149 there were no changes in metabolites associated with the gluconeogenesis pathway (Fig.
150 2B). Although pyruvate was added as part of the LPO cocktail, increased pyruvate
151 generation also occurred as a result of increased lactate dehydrogenase activity (Fig. 2C).
152 Although we were unable to directly measure oxaloacetate levels, we used aspartate as a
153 surrogate and found increased m+3 labelling, demonstrating direct conversion between
154 these two metabolites (Fig. 2D). Furthermore, isotopomer labelling of citrate indicated
155 preferential synthesis from oxaloacetate and decreased conversion of labelled acetyl-CoA
156 by PDH (Fig. 2E). An alternative pathway for pyruvate is conversion to alanine and whilst
157 there were no changes in steady state alanine levels, there were moderate, but significant,
158 changes in the incorporation of ^{13}C (Fig. 2F), indicating sustained interconversion of these
159 two metabolites. Despite there being no increase in steady state levels of gluconeogenesis-
160 associated metabolites, the increased m+2 labelling of 3-PG (Fig. 2G), serine (Fig. 2H), and
161 glycine (Fig. 2I), suggests increased flux through the gluconeogenesis pathway.

162

163 **Steatosis in HLCs is associated with truncation of the TCA cycle**

164 Isotopic labelling of TCA metabolites can produce a number of different isotopomers,
165 dependent on the directionality of metabolite synthesis (Fig. 3A). In steatotic HLCs, we
166 observed increases in steady state levels of the TCA cycle metabolites αKG , fumarate and
167 malate (Fig. 3B). In contrast, there were no changes in the steady state levels of succinate
168 and no evidence for increased cataplerosis through glutamate. To further analyse alterations
169 in TCA cycle dynamics we measured ^{13}C incorporation into metabolites. Whilst there was

170 increased ^{13}C incorporation into PC-derived citrate (Fig. 2E), this was not the case for αKG
171 (Fig. 3C). The decreased levels of ^{13}C incorporation into glutamate demonstrates that this
172 does not result from increased cataplerosis through glutamate (Fig. 3D). The increased
173 expression of OGDHL and decreased expression of SUCG1 (Table S2) suggest that
174 steatosis is associated with the generation of an increased pool of succinyl-CoA, with
175 impaired conversion to succinate. This is supported by substantially decreased incorporation
176 of ^{13}C into succinate (Fig 3E). In contrast, we observed increased ^{13}C incorporation into
177 fumarate, malate, and aspartate (Fig 3F & 3G). Since malate dehydrogenase and fumarate
178 hydratase readily reverse their reactions (Dasika et al., 2015; Tyrakis et al., 2017), increased
179 incorporation of ^{13}C into both malate and fumarate indicate a reversal of TCA cycle activity.
180 Taken together, this shows that truncation of the TCA cycle occurs in steatotic cells, with
181 inhibition of the conversion of succinate to fumarate (Fig. 3H). The increased incorporation
182 of ^{13}C into oxaloacetate (using aspartate as a surrogate), demonstrates increased PC
183 activity, driving the conversion of pyruvate to oxaloacetate and suggests possible disruption
184 of associated metabolic cycles, including the malate-aspartate shuttle (MAS) and the purine
185 nucleotide cycle (PNC).

186

187 **Increased PNC and MAS activity drives NAFLD-associated fumarate accumulation**

188 Next, we wanted to determine the source of fumarate accumulation in steatotic HLCs.
189 Transcriptomic analysis identified dysregulation of multiple genes associated with the MAS
190 (Fig. 4A) and PNC (Fig. 4B), indicating that these pathways may be involved in fumarate
191 accumulation. To investigate this further, HLCs incubated with $^{13}\text{C}_3$ -lactate-labelled LPO
192 were co-incubated with either 5-Aminoimidazole-4-carboxamide-1- β -D-ribofuranosyl 5'-
193 monophosphate (AICAR) or O-(Carboxymethyl)hydroxylamine hemihydrochloride (AOA), to
194 inhibit the PNC or MAS, respectively. Addition of AICAR increased only the steady state
195 levels of αKG , and neither AICAR nor AOA had a significant impact on the synthesis of
196 pyruvate, citrate, succinate or malate (Fig. 4C). However, both inhibitors significantly

197 reduced steady state levels of fumarate and aspartate. Whilst addition of AICAR did not
198 impact on the synthesis of PDH-derived citrate (Fig. 4D), it did result in increased
199 accumulation of PDH-derived ^{13}C in αKG (Fig. 4E), suggesting impaired conversion to
200 succinyl-CoA or increased anaplerosis from glutamate. AICAR was also able to partially
201 restore the effects of steatosis on succinate levels (Fig. 4F), resulting in small but significant
202 increases in PC- and PDH-derived isotopomers. The most profound effect of AICAR was on
203 fumarate, with each isotopomer reduced to levels below those observed in the control group
204 (Fig. 4G), demonstrating that in steatotic HLCs, fumarate accumulation is primarily driven by
205 the PNC. Following AOA treatment, we observed a moderate decrease in PC-derived ^{13}C
206 incorporation into fumarate, demonstrating a small contribution from the MAS. AICAR had a
207 moderate impact on incorporation of PC-derived incorporation of ^{13}C into malate, whereas
208 AOA impacted on both PC- and PDH-derived ^{13}C incorporation, suggesting limited
209 contribution of the MAS and PNC to malate accumulation (Fig. 4H). Both AICAR and AOA
210 reduced incorporation of ^{13}C into aspartate (Fig. 4I). These data show that in the presence of
211 TCA cycle truncation, mitochondria increase both MAS and PNC activity (Fig. 4J).

212

213 **Inhibition of fumarate accumulation inhibits lipid droplet hypertrophy in LPO-treated
214 HLCs**

215 To determine whether manipulation of fumarate levels affected the development of
216 macrovesicular steatosis, we performed HCA microscopy on HLCs. Cells treated with LPO
217 and AICAR did not develop macrovesicular steatosis (Fig. 4K). The addition of exogenous
218 fumarate to steatotic HLCs treated with AICAR resulted in the development of larger lipid
219 droplets.

220

221 **Fumarate accumulation is not associated with widespread alterations of 5hmC in
222 protein-coding regions in steatotic HLCs**

223 As we observed increased synthesis of fumarate in steatotic HLCs, we aimed to determine
224 whether this would impact on TET enzyme activity, as determined by changes in 5hmC. To

225 do so we carried out genome-wide 5hmC sequencing, identifying 3294 differentially
226 hydroxymethylated regions (DHRs) between LPO exposed and control cells (>2-fold change,
227 see methods). Within each group, samples were highly correlated, suggesting that the 5hmC
228 patterns are stable between replicate samples (Fig. 5A), with the majority of change located
229 in intragenic or intronic regions (Fig. 5B). It is thought that 5hmC in gene body regions may
230 functionally relate to mRNA transcription (Thomson et al., 2016). Therefore, we generated
231 heatmaps representing mean changes across the gene body, with cluster 1 showing subtle
232 increases in 5hmC within the TSS region (Fig. 5C). Analysis of genic 5hmC patterns reveal
233 that a number of promoter regions display changes in 5hmC levels following LPO exposure.
234 (Fig. 5D). In line with this, we integrated DHR and RNA-seq data to look at promoter regions
235 upstream of the transcriptional start site. In doing so, we identified 12 promoter regions with
236 differential enrichment of 5hmC (>2-fold) and where mRNA expression was altered >0.5-
237 fold. Linear regression of these regions identified a moderate but significant negative
238 relationship between 5hmC enrichment and mRNA expression (Fig. S1; Table S4). Of these
239 genes 7 (EPHX3, ERO1B, CSGALNACT1, DOC2A, COL6A1, CASP1 and TMEM88) were
240 previously shown to be dysregulated in the pathogenesis of NAFLD or progression to
241 cirrhosis (Atanasovska et al., 2017; Cazanave et al., 2017; Parafati et al., 2018; Revill et al.,
242 2013; Wilson and Kumar, 2018). This may indicate a role for 5hmC in the regulation of these
243 genes in NAFLD pathogenesis.

244

245

246

247

248

249

250

251

252

253 **Discussion**

254 NAFLD is a challenging disease to study in humans. This is due to the difficulty of obtaining
255 tissues that are not compromised by confounding conditions which make high resolution
256 analysis of transcriptional and metabolic rewiring difficult. Using this HLC-based model of
257 NAFLD we were able to overcome many of these difficulties.

258

259 Through transcriptomic analysis, we observed disruption of the expression of genes in
260 multiple pathways related to metabolism, confirming the findings of a number of previous
261 studies in humans and mouse (Collison et al., 2009; Hardwick et al., 2013; Kolwankar et al.,
262 2007; Liu et al., 2016; Nikolaou et al., 2019; Schiöth et al., 2016; Suppli et al., 2019;
263 Yamaguchi and Murata, 2013). Previous studies in mouse models and indirect studies in
264 humans have reported increases in hepatic TCA cycle activity associated with NAFLD
265 (Satapati et al., 2012, 2015; Sunny et al., 2011). Additionally, compromised ETC activity with
266 decreased mitochondrial maximal respiration has been reported in response to hepatic
267 steatosis (Koliaki et al., 2015; Sinton et al., 2020). However, it was unclear whether impaired
268 maximal respiration is solely due to downregulation of respiratory chain units or whether this
269 is, in part, due to chemical inhibition of complexes I-III by octanoic acid, as previously
270 described in rat liver (Scaini et al., 2012). Our transcriptomic analysis revealed substantial
271 disruption of TCA cycle and oxidative phosphorylation pathways, indicating compromised
272 energy metabolism in HLCs. In particular, our findings that transcription of multiple subunits
273 of respiratory complexes I, IV and ATPase were downregulated suggest that transcription-
274 based disruption of the ETC plays a role in impaired respiration.

275

276 Traditionally, NAFLD is also thought to increase TCA cycle activity (Satapati et al., 2012;
277 Sunny et al., 2011) but, to date, detailed information regarding flux dynamics has remained
278 elusive. We utilised stable isotopic tracing, using $^{13}\text{C}_3$ -lactate which provides greater
279 metabolite labelling than other substrates (Hui et al., 2017). In the liver, flux of substrates
280 into the TCA cycle predominantly occurs via PC (Lardy et al., 1965), and there is evidence

281 suggesting that PC activity increases in NAFLD (Sunny et al., 2011), and contributes to
282 increased rates of gluconeogenesis through conversion of oxaloacetate to
283 phosphoenolpyruvate (Satapati et al., 2012). The data presented here support the assertion
284 that PC activity increases in steatotic cells. However, while we observed sustained synthesis
285 of gluconeogenesis-associated metabolites occurring in steatotic HLCs, our data show no
286 associated increase in gluconeogenesis. Increased incorporation of only two ¹³C atoms into
287 each of these metabolites may suggest that pyruvate-derived acetyl-CoA is being converted
288 back to pyruvate *via* ketogenesis before entering gluconeogenesis. Increased acetyl-CoA
289 pools and disrupted ketogenesis have been observed in NAFLD (Fletcher et al., 2019),
290 lending support to this assertion. This demonstrates that pyruvate is predominantly being
291 utilised to sustain TCA cycle activity in steatotic HLCs.

292

293 The increased flux of substrates into the TCA cycle also leads to higher levels of TCA cycle
294 activity, as previously reported (Sunny et al., 2011). However, our data show that changes in
295 TCA cycle are more nuanced than was previously suggested. We identified a truncation of
296 the TCA cycle, with inhibition of the conversion of succinate to fumarate. This raised the
297 question of why less ¹³C is being incorporated into succinate. The lack of cataplerosis
298 through glutamate suggests that this is due to diminished conversion of succinyl-CoA to
299 succinate and generation of an increased pool of succinyl-CoA. This is supported by the
300 observation of decreases in PC-derived glutamate and succinate, despite no changes in PC-
301 derived α KG. Since interconversion between succinyl-CoA and succinate is in near
302 equilibrium and readily reversible (Lynn and Guynn, 1978), we propose that this effect could
303 be a result of diminished succinyl-CoA synthetase activity.

304

305 Despite truncation of the TCA cycle, we found that HLCs are able to rewire their metabolic
306 circuitry to compensate for this, generating increased levels of fumarate, predominantly
307 through the PNC, and to a lesser extent the MAS. A similar metabolic bypass has been
308 reported in cardiac ischemia (Chouchani et al., 2014), as well as human and mouse *in vitro*

309 models of tumorigenesis (Tyrakis et al., 2017). In ischemic reperfusion injury, increased
310 PNC activity results in fumarate overflow, driving reversal of succinate dehydrogenase
311 activity and accumulation of succinate (Chouchani et al., 2014). We did not observe the
312 same phenomenon here, but rather found evidence for inhibition of succinate
313 dehydrogenase activity in steatotic HLCs. Although it is possible for fumarate to be
314 generated from reversal of fumarate hydratase (FH) activity (Chouchani et al., 2014), we
315 were unable to directly manipulate the activity of this enzyme in order to assess its
316 contribution to the fumarate pool in steatotic HLCs. However, as FH operates at equilibrium
317 (Ajalla Aleixo et al., 2019) it is possible that PNC-fuelled fumarate accumulation prevents
318 reverse catalytic activity. Defects in complex I can lead to a reduction in the levels of NAD⁺
319 (Porcelli et al., 2010) and regeneration of fumarate via the PNC may be one mechanism of
320 increasing the NADH pool and maintaining the hydrogen ion gradient of the ETC. The
321 synthesis of fumarate by the PNC also results in the generation of AMP, which in turn is
322 deaminated to produce ammonia (Arinze, 2005). In rodents, hyperammonaemia is
323 associated with the progression of hepatic steatosis to cirrhosis (De Chiara et al., 2020), and
324 our findings suggest that this is generated through increased PNC activity. This leads to the
325 question of whether NAFLD-associated cirrhosis is then a consequence of ammonia
326 production or a downstream effect of fumarate accumulation.

327
328 A further consequence of fumarate accumulation is the development of macrovesicular
329 steatosis. Inhibition of the PNC prevented development of macrovesicular lipid droplets, and
330 this was partially restored following the addition of exogenous fumarate. This correlates with
331 findings in oligodendrocytes and CD8+ T cells, in which exposure to exogenous fumarate
332 resulted in perturbed lipid metabolism (Bhargava et al., 2019; Huang et al., 2015), although
333 the mechanism by which this occurs remains unknown. However, our data suggest that
334 fumarate is important for the development of macrovesicular steatosis in HLCs and that
335 mechanisms compensating for TCA cycle truncation in LPO-treated HLCs cells drive
336 intracellular lipid accumulation.

337

338 Another potential consequence of fumarate accumulation in steatotic HLCs was inhibition of
339 α KG-dependent dioxygenase enzyme activity. Given our previous data showing altered
340 5hmC in a mouse model of NAFLD and the potential importance of the TET enzymes in
341 hepatocellular carcinoma (Lyall et al., 2020; Thomson et al., 2016), we used a DIP-seq
342 approach to measure changes in 5hmC across the genome. 5hmC is a stable epigenetic
343 modification and may influence transcription, and while the nature of this influence is unclear
344 studies suggest that 5hmC enrichment at transcriptional start sites (TSSs) leads to
345 repression of transcription (Wu et al., 2011). Recent studies in mice showed that 5hmC
346 enrichment is reversibly altered at specific loci in response to fat accumulation in the liver,
347 indicating that the TET enzymes may play a role in NAFLD pathogenesis (Lyall et al., 2020).
348 We did not observe wide-scale changes in 5hmC enrichment, and 5hmC changes at specific
349 loci did not, in general, correlate with transcriptional changes in steatotic cells, except at a
350 limited number of promoter regions. As NAFLD comprises a spectrum of pathologies, it is
351 possible that our model reflects a different disease stage or that the changes in other studies
352 are a consequence of the use of whole tissue. It is also possible that differential 5hmC
353 enrichment is occurring in regions associated with expression of non-coding RNAs, including
354 long noncoding RNAs or microRNAs, which in turn may influence mRNA transcription (Hu et
355 al., 2017; Wang et al., 2019a). Other mechanisms by which fumarate, as an allosteric
356 inhibitor of the dioxygenase family of enzymes may impact on transcriptional regulation in
357 NAFLD, include through effects on HIF1 α or the histone demethylase enzymes (Han et al.,
358 2019; Kim et al., 2018).

359

360 Taken together, we demonstrate for the first time that the development of steatosis in HLCs
361 associates with truncation of the TCA cycle. We further demonstrate that on exposure to
362 LPO, mitochondrial metabolic pathways are re-wired in order to maintain TCA cycle activity,
363 through PNC-driven fumarate accumulation, which then results in the development of

364 macrovesicular steatosis. These findings reveal a previously unknown mechanism linked to
365 hepatic steatosis and may lead to further understanding of transcriptional and metabolic
366 rewiring associated with NAFLD.

367

368 **Acknowledgements:**

369 MCS was supported by a British Heart Foundation PhD studentship (FS/16/54/32730) and
370 by the British Heart Foundation Centre of Research Excellence. SW-Z was funded by the
371 Deutsche Forschungsgemeinschaft (SFB960). This work was supported in part by the
372 Wellcome Trust [grant number 208400/Z/17/Z] and we thank HWB-NMR at the University of
373 Birmingham for providing open access to their Wellcome Trust-funded NMR equipment. AJD
374 was funded by the British Heart Foundation Centre of Research Excellence, University of
375 Edinburgh. Our thanks go to the Wellcome Trust Clinical Research Facility Genetics Core,
376 Western General Hospital, Edinburgh, UK. DCH, JMR, BLV were supported with awards
377 from the MRC Doctoral Training Partnership (MR/K501293/1) and the Chief Scientist Office
378 (TCS/16/37).

379

380 **Data Accessibility:**

381 Transcriptomic sequencing data have been deposited on the GEO repository (accession
382 number GSE138052). 5hmC sequencing data have also been deposited on the GEO
383 repository (accession number GSE144955).

384

385 **Author Contributions:**

386 MCS was involved in conceptualisation, methodology, validation, formal analysis,
387 investigation, data curation, writing (original draft preparation, reviewing and editing) and
388 visualisation. BLV, JMR, PDW and AT were involved in methodology, validation, formal
389 analysis, investigation and writing (reviewing and editing). SW-Z and JPT were involved in
390 software, formal analyses, data curation and writing (reviewing and editing). CL and DAT
391 were involved in conceptualisation, methodology, validation, formal analysis, investigation,

392 data curation, provision of resources, writing (reviewing and editing), project administration,
393 funding acquisition and supervision. DCH and AJD were involved in conceptualisation,
394 methodology, validation, formal analysis, provision of resources, writing (reviewing and
395 editing), project administration, funding acquisition and supervision.

396

397 **Declaration of interests:**

398 Professor David Hay is a founder, shareholder and director in Stemnovate Limited.

399

400

401

402 **Figure Legends**

403 **Figure 1.** LPO treatment induces macrovesicular steatosis in HLCs, which is associated with
404 transcriptional rewiring reflecting human NAFLD. **(A)** Intracellular lipid droplets increase in
405 size in response to LPO ($n = 24$ (control) and 20 (LPO) biological replicates/group). **(B)**
406 Heatmap analysis of transcriptional changes associated with macrovesicular steatosis. **(C)**
407 Expression of key NAFLD-associated genes is disrupted in steatotic HLCs. **(D-E)** Pathway
408 enrichment analysis reveals a number of disrupted pathways associated with macrovesicular
409 steatosis. **(F-G)** Analysis of KEGG TCA cycle and oxidative phosphorylation pathways
410 reveals extensive disruption of expression of key genes. Data in **(A)** were analysed using a
411 two-tailed Student's t-test. Data in **(C)** were analysed by two-way ANOVA with Sidak post-
412 hoc testing. Unless otherwise specified, $n = 3$ biological replicates per group. Data are
413 expressed as mean \pm SD.

414

415 **Figure 2.** Macrovesicular steatosis is associated with increased PC activity, leading to
416 preferential anaplerosis of pyruvate into the TCA cycle. **(A)** Schematic outlining conversion
417 of lactate to pyruvate and routes by which this can be converted. Black circles denote
418 carbon atoms. **(B)** Steady state measurements of pyruvate and metabolites that it can be
419 converted to. Isotopomer labelling patterns of pyruvate **(C)**, aspartate **(D)** and citrate **(E)**
420 show anaplerosis into the TCA cycle. There is minimal conversion of pyruvate to alanine **(F-**
421 **G)**, but increased flux of the $m+2$ isotopomer through metabolites related to
422 gluconeogenesis, with sustained conversion to 3-PG, serine and glycine **(H-K)**. For NMR
423 data, labels are: 1 = ^{13}C labelling; 0 = no ^{13}C labelling. All GC-MS data consisted of 10
424 biological replicates and 2 technical replicates. Isotopomer data were calculated by
425 multiplying MID (multiple ion detection) by normalised total ion count. For NMR data **(G and**
426 **K)** $n = 4$ biological replicates/group. Data were analysed by two-way ANOVA with Sidak
427 post-hoc testing, or **(I-J)** two-tailed Student's t-test. Data are expressed as mean \pm SD.

428 **Figure 3.** Macrovesicular steatosis in HLCs results in truncation of the TCA cycle, inhibiting
429 conversion of succinate to fumarate. Paradoxically, this is associated with increased

430 accumulation of fumarate. **(A)** Schematic outlining the TCA cycle and possible ^{13}C labelled
431 isotopomers from a single cycle. **(B)** Steady state measurements of TCA cycle-associated
432 metabolites that could be measured by GC-MS. **(C)** PC-derived αKG is unchanged in the
433 presence of steatosis, and PDH-derived αKG is reduced. **(D-E)** Labelling patterns of αKG
434 are not due to increased cataplerosis through glutamate, as both PC- and PDH-derived
435 glutamate are reduced in response to steatosis. **(F)** Furthermore, reduced ^{13}C labelling of
436 succinate indicates inefficient conversion from αKG . **(G-H)** Despite reduced labelling of
437 succinate, both fumarate and malate show increased PC-derived label incorporation. **(I)**
438 Proposed model of preferential anaplerosis of pyruvate into the TCA cycle, with concomitant
439 truncation, preventing conversion of succinate to fumarate. For NMR data, labels are: 1 =
440 ^{13}C labelling; 0 = no ^{13}C labelling. All GC-MS data consisted of 10 biological replicates and 2
441 technical replicates. Isotopomer data were calculated by multiplying MID (multiple ion
442 detection) by normalised total ion count. For NMR data **(E)** $n = 4$ biological replicates/group.
443 Data were analysed by two-way ANOVA with Sidak post-hoc testing and are expressed as
444 mean \pm SD.

445

446 **Figure 4.** In the presence of TCA cycle truncation, the purine nucleotide cycle and malate-
447 aspartate shuttle fuel fumarate accumulation. **(A-B)** Transcriptomic analysis showed
448 increased expression of malate-aspartate shuttle (MAS) and purine nucleotide cycle (PNC)
449 transcripts, indicating perturbed activity. **(C)** Inhibition of the PNC and MAS reversed
450 steatosis-induced accumulation of fumarate and aspartate, but not malate. **(D)** PNC
451 inhibition moderately impacted PC-derived citrate ^{13}C labelling, but not **(E)** αKG or **(F)**
452 succinate. **(G)** In contrast, PNC inhibition profoundly reduced incorporation of ^{13}C into
453 fumarate. MAS inhibition also limited PC-derived fumarate accumulation, but to a lesser
454 extent. **(H)** PNC and MAS expression also inhibited generation of PC-derived malate, but to
455 a much smaller extent than fumarate. **(I)** PNC and MAS inhibition also resulted in a
456 significant reduction in the generation of PC-derived aspartate. **(J)** Schematic outlining the

457 proposed pathways by which fumarate accumulation occurs in response to steatosis. (K)
458 Inhibition of fumarate through the PNC reduced LPO-induced macrovesicular steatosis,
459 which was partially restored through addition of exogenous monomethyl fumarate. For NMR
460 data, labels are: 1 = ^{13}C labelling; 0 = no ^{13}C labelling. AICAR = PNC inhibitor; AOA = MAS
461 inhibitor. All Control and LPO group GC-MS data consisted of 10 biological replicates and 2
462 technical replicates, as shown in Figure 3. GC-MS LPO + AICAR and LPO + AOA groups
463 consisted of 6 biological replicates/group. Isotopomer data were calculated by multiplying
464 MID by normalised total ion count. For lipid droplet analysis (K), the LPO group is as shown
465 in Figure 1. For the LPO + AICAR and the LPO + AICAR + Fumarate group, $n = 31$ and 28
466 biological replicates/group, respectively. Data were analysed by two-way ANOVA with Sidak
467 post-hoc testing and are expressed as mean \pm SD.

468

469 **Figure 5.** Macrovesicular steatosis in HLCs does not correlate with wide-scale changes in
470 5hmC enrichment. (A) Correlation heatmap of control vs. LPO groups, following hmeDIP
471 sequencing, clustered by Euclidean distance. (B) Proportion of DHRs associated with
472 different regions of the genome, showing the majority located in intragenic and intronic
473 regions. (C) Heatmap of DHRs, with an FDR of <0.05 and k-means clustering. (D) Sliding
474 window analysis of the transcriptional start site (TSS), gene body, and transcriptional end
475 site (TES) shows minimal changes between control and LPO groups. For both control and
476 LPO, $n = 3$ biological replicates/group.

477

478

479

480

481

482

483

484

485 **Materials and Methods**

486 **Differentiation of pluripotent human stem cells to hepatocyte-like cells and induction**
487 **of intracellular lipid accumulation**

488 Human female H9 pluripotent stem cells (PSCs) were differentiated to hepatocyte-like cells
489 (HLCs) as previously described (Wang et al., 2017). HLCs were cultured in a 96-well format
490 for measurements of lipid accumulation and in a 6-well format for all other analyses. To
491 assess loss of pluripotency and development of a gain of a hepatocyte-like phenotype, we
492 measured expression of pluripotency (NANOG) and hepatocyte (ALB, HNF4A) markers
493 throughout the differentiation process (Fig. S1A). Details of primers and Universal Probe
494 Library probes (Roche) can be found in Table S1. CYP3A4 activity was similar to that
495 previously observed, demonstrating that HLCs are functionally similar to hepatocytes (Wang
496 et al., 2017), and this was not diminished by intracellular lipid accumulation (Fig. S1B). Lipid
497 accumulation was induced as previously described (Lyall et al., 2018). Briefly, at day 17,
498 HLCs were exposed to a cocktail of sodium l-lactate (L; 10mM), sodium pyruvate (P; 1 mM)
499 and octanoic acid (O; 2 mM) (Sigma, Gillingham, UK) for a period of 48 h. For isotopic
500 tracing studies, lactate was replaced with ¹³C₃-lactate (CK Isotopes, CLM-1579-05). For
501 mechanistic studies, HLCs were exposed to either 5-Aminoimidazole-4-carboxamide-1-β-D-
502 ribofuranosyl 5'-monophosphate (AICAR; 1mM; Sigma-Aldrich, A1393-50MG), O-
503 (Carboxymethyl)hydroxylamine hemihydrochloride (AOA; 100 μM ; Sigma-Aldrich, C13408-
504 1G) or AICAR combined with monomethyl fumarate (50 μM; Sigma-Aldrich, 651419-1G) for
505 the same duration as LPO.

506

507 **RNA-seq analysis**

508 Total RNA was extracted from HLCs using the Monarch® Total RNA Miniprep Kit (New
509 England BioLabs, T2010). RNA integrity was assessed using a Bioanalyzer (Agilent) with
510 the RNA 6000 Nano kit. All samples had a RIN value >7.0. mRNA sequencing was
511 performed on 3 biological replicates per group by the Beijing Genomics Institute (BGI)

512 (Shenzhen, China). Library preparation was performed with the TruSeq Stranded mRNA
513 Library Preparation kit (Illumina, RS-122-2101), with additional use of the Ribo-Zero Gold
514 rRNA Removal Kit (Illumina, MRZG12324). Paired-end sequencing was performed on an
515 Illumina HiSeq 4000, with each sample sequenced to a depth >90 million reads. The
516 generated FASTQ files were trimmed to remove adapters, using Trimmomatic (version 0.36)
517 (Bolger et al., 2014), before performing quality control with FastQC (version 0.11.4)
518 (Andrews). Alignment was performed against the *Homo sapiens* GRCh19 assembly. The
519 assembly was first indexed using STAR (version 2.5.1b) before mapping trimmed reads,
520 using STAR (version 2.5.1b) in paired-end mode with default behaviour (Dobin and
521 Gingeras, 2015). Duplicate reads were removed using Picard (version 2.7.11) (2018), before
522 using featureCounts to generate raw read counts for each gene. Differential gene
523 expression (DEG) analysis was performed using DESeq2 (Love et al., 2014). Heatmaps
524 were generated with Heatmapper (Babicki et al., 2016). Pathway enrichment analysis was
525 performed using the Kyoto Encyclopedia of Genes and Genomes (KEGG) function
526 (Kanehisa, 2019; Kanehisa and Goto, 2000; Kanehisa et al., 2019) of the Database for
527 Annotation, Visualization, and Integrated Discovery (DAVID) (Huang et al., 2009a, 2009b).

528

529 **Real-time quantitative PCR**

530 RNA was taken from that prepared for RNA-sequencing. cDNA was generated using the
531 High Capacity cDNA Reverse Transcriptase Kit (Applied Biosystems, 4368814). A master
532 mix was prepared using PerfeCTa FastMix II (Quanta Biosciences, Inc., 95118-250). cDNA
533 was amplified and quantified using the Universal Probe Library (Roche, Burgess Hill, UK)
534 system on a Roche LightCycler 480 (Roche Diagnostics Ltd, Switzerland).

535

536 **NMR Spectroscopy**

537 This protocol was previously described by Hollinshead *et al* (Hollinshead et al., 2018). At the
538 conclusion of tracer experiments, cells were washed with 2 mL ice-cold 0.9% saline solution
539 and quenched with 0.3 mL pre-chilled methanol (-20 °C). After adding an equal volume of

540 ice-cold HPLC-grade water containing 1 μ g/mL D6-glutaric acid (C/D/N Isotopes Inc), cells
541 were collected with a cell scraper and transferred to tubes containing 0.3 mL of chloroform (-
542 20 °C). The extracts were shaken at 1400 rpm for 20 min at 4 °C and centrifuged at 16,000 x
543 g for 5 min at 4 °C. Then, 0.3 mL of the upper aqueous phase was collected and evaporated
544 in eppendorfs, under a vacuum using a Savant™ SpeedVac™ Concentrator (ThermoFisher).
545 These samples were used either for NMR spectroscopy or for GC-MS. For NMR, dried
546 samples were re-suspended in 60 μ L of 100 mM sodium phosphate buffer (pH 7.0)
547 containing 500 μ M DSS and 2 mM Imidazole, 10% D2O, pH 7.0. Samples were vortexed,
548 sonicated (5-15 min) and centrifuged briefly, before transferred to 1.7 mm NMR tubes using
549 an automated Gilson. One-dimensional (1D)- 1 H NMR spectra and two-dimensional (2D)-
550 1 H, 13 C Heteronuclear Single Quantum Coherence Spectroscopy (HSQC) NMR spectra were
551 acquired using a 600 MHz Bruker Avance III spectrometer (Bruker Biospin) with an inverse
552 cryogenic probe for 1.7 mm NMR sample tubes, fitted with a z-axis pulsed field gradient, at
553 300 K. Spectral widths were set to 13 and 160 ppm for the 1 H and 13 C dimensions,
554 respectively. For the indirect (13 C) dimension of the 2D- 1 H, 13 C HSQC NMR spectra, 1228 out
555 of 4096 (30%) data points were acquired using a non-uniform sampling scheme. 13 C- 13 C
556 splittings were enhanced 4-fold in the 13 C dimension. Each sample was automatically tuned,
557 matched and then shimmed (1D-TopShim) to a DSS line width of <1 Hz before acquisition of
558 the first spectrum. Total experiment time was ~15 min per sample for 1D- 1 H NMR spectra
559 and 1 h per sample for 2D- 1 H, 13 C HSQC NMR spectra. 1D- 1 H NMR spectra were processed
560 using the MATLAB-based MetaboLab software (Ludwig and Günther, 2011). All 1D data
561 sets were apodized using a 0.3 Hz exponential window function and zero-filled to 131,072
562 data points before Fourier Transformation. The chemical shift was calibrated by referencing
563 the DSS signal to 0 ppm. 1D- 1 H NMR spectra were manually phase corrected. Baseline
564 correction was achieved using a spline function (Ludwig and Günther, 2011). 1D- 1 H-NMR
565 spectra were exported into Bruker format for metabolite identification and concentration
566 determination using Chenomx 7.0 (Chenomx INC). 2D- 1 H, 13 C HSQC NMR spectra were

567 reconstructed using compressed sensing in the MDDNMR and NMRpipe software (Delaglio
568 et al., 1995; Kazimierczuk and Orekhov, 2011; Orekhov and Jaravine, 2011). The final
569 spectrum size was 922 real data points for the ^1H dimension and 16,384 real data points for
570 the ^{13}C dimension. Analysis was performed using MetaboLab and pyGamma software was
571 used in multiplet simulations (Smith et al., 1994). The methyl group of lactate was used to
572 calibrate the chemical shift based on its assignment in the human metabolome database
573 (Wishart et al., 2013).

574

575 **GC-MS**

576 Dried polar metabolites were purified as described for NMR spectroscopy. These were
577 derivatised by incubating with 40 μL 2% methoxyamine hydrochloride (Sigma Aldrich,
578 226904) in pyridine (Thermo Fisher Scientific, 25104) at 60 $^{\circ}\text{C}$ for 1 h, followed by incubation
579 with 60 μL *N*-methyl-*N*-*tert*-butyldimethylsilyltrifluoroacetamide with 1% *tert*-
580 butyldimethylchlorosilane (MTBSTFA with 1% t-BDMCS) at 60 $^{\circ}\text{C}$ for 1 h.

581

582 GC-MS analysis was performed using an Agilent 6890GC in combination with an Agilent
583 5975C MS. The MS was operated under electron impact ionization at 70 eV with the source
584 held at 230 $^{\circ}\text{C}$ and the quadrupole at 150 $^{\circ}\text{C}$. Helium was used as the carrier gas and
585 maintained at a flow rate of 1 mL/min. 1 μL of derivatised sample was injected (splitless) with
586 an inlet temperature of 280 $^{\circ}\text{C}$ on to a Rxi-5MS column (Restek) The oven temperature was
587 held at 100 $^{\circ}\text{C}$ for 1 min then increased at a rate of 5 $^{\circ}\text{C}/\text{min}$ up to a maximum temperature
588 of 330 $^{\circ}\text{C}$. Ions were detected using selected ion monitoring (SIM) mode as previously
589 described (Battello et al., 2016). MetaboliteDetector software was used to correct for the
590 natural isotope distribution and to determine the mass isotopomer distribution (MID) (Hiller et
591 al., 2009).

592

593

594 **DNA hydroxymethylation immunoprecipitation and sequencing (hmeDIP-sequencing)**

595 DNA was purified using the Monarch® Genomic DNA Purification kit (New England BioLabs,
596 T3010S). DNA immunoprecipitation and sequencing was performed as previously described,
597 using the Ion Proton platform (Thomson et al., 2015), with the addition of an IgG control
598 (Merck, 12-370). We sequenced three biological replicates per group. A mean read length of
599 137-147 base pairs and 21,130,039 - 31,693,844 reads per sample was achieved. Reads
600 were aligned to the hg19 genome using Torrent Suite v5.2.0. Aligned reads were sorted
601 using SAMtools, before calling peaks using MACS2 (v. 2.1.1) -f BAM --broad --broad-cutoff
602 0.05 -B -g hs, over corresponding inputs (Zhang et al., 2008). To detect differentially
603 hydroxymethylated regions (DHRs), we used Diffbind with DESeq2 (Stark and Brown). For
604 Diffbind analysis, data were normalised to a pooled input for each group and an IgG control.
605 DHMRs were assigned to genes and other genomic features using the HOMER (v. 4.8;
606 hg19) annotatePeaks tools (Heinz et al., 2010). For candidate hmeDIP analysis, the
607 concentration of each sample was extrapolated from a standard curve of arbitrary
608 concentrations and normalised to 10% input. Regions of interest were identified from the
609 hmeDIP-sequencing dataset. Primers were designed using the NCBI primer-BLAST
610 software (Table S2). Data are available through the Gene Expression Omnibus
611 (GSE144955). Sliding window profiles and heatmaps were generated using deepTools
612 (Ramírez et al., 2014), using the plotProfile and plotHeatmap functions, respectively, with
613 blacklisted regions subtracted.

614

615 **High content analysis microscopy**

616 Cells were stained with a cell painter assay, adapted from Lyall *et al* and Bray *et al* (Bray et
617 al., 2016; Lyall et al., 2018). Cells were fixed with 50 µL/well 4% (wt/vol) paraformaldehyde
618 (Electron Microscopy Sciences, 15710-S) for 15 minutes at room temperature. For
619 permeabilisation, cells were incubated in 0.1% Triton X-100 (Sigma-Aldrich, T8787) in PBS
620 for 15 minutes at room temperature. For lipid droplet analysis, cells were then stained with a
621 combination of NucBlue Live ReadyProbes® Reagent (2 drops/mL) (Molecular Probes,

622 R37605), HCS CellMask™ Red (2 μ L/10 mL) (Invitrogen, H32712), and BODIPY™ 493/503
623 (1:1000) (Life Sciences, D3922), as per the manufacturer's instructions. Following staining,
624 images were acquired using an Operetta High Content Analysis microscope (Perkin Elmer,
625 Buckinghamshire, UK). Lipid droplet morphology was analysed as previously described
626 (Lyall et al., 2018).

627

628 **Statistical analysis**

629 All statistical analyses were performed using Graph Prism Version 8.0 for Windows or
630 macOS, GraphPad Software, La Jolla California USA, www.graphpad.com. Normality of
631 data distribution was measured using the Shapiro-Wilks test. Where indicated, data were
632 analysed by unpaired Student's t-test, Mann-Whitney test, one-way analysis of variance
633 (ANOVA) or two-way ANOVA. Data were considered to be significant where $p < 0.05$.

634

635

636

637

638

639

640

641

642

643

644

645

646

647

648

649

650 **References**

651 Ajalla Aleixo, M.A., Rangel, V.L., Rustiguel, J.K., de Pádua, R.A.P., and Nonato, M.C.
652 (2019). Structural, biochemical and biophysical characterization of recombinant human
653 fumarate hydratase. *FEBS J.* **286**, 1925–1940.

654 Andrews, S. FastQC: a quality control tool for high throughput sequence data.

655 Antoniewicz, M.R. (2018). A guide to ¹³C metabolic flux analysis for the cancer biologist.
656 *Exp. Mol. Med.* **50**, 19.

657 Arinze, I.J. (2005). Facilitating understanding of the purine nucleotide cycle and the one-
658 carbon pool: Part I: The purine nucleotide cycle. *Biochem. Mol. Biol. Educ.* **33**, 165–168.

659 Asrih, M., and Jornayvaz, F.R. (2015). Metabolic syndrome and nonalcoholic fatty liver
660 disease: Is insulin resistance the link? *Mol. Cell. Endocrinol.* **418**, 55–65.

661 Atanasovska, B., Rensen, S.S., van der Sijde, M.R., Marsman, G., Kumar, V., Jonkers, I.,
662 Withoff, S., Shiri-Sverdlov, R., Greve, J.W.M., Faber, K.N., et al. (2017). A liver-specific long
663 noncoding RNA with a role in cell viability is elevated in human nonalcoholic steatohepatitis.
664 *Hepatology* **66**, 794–808.

665 Babicki, S., Arndt, D., Marcu, A., Liang, Y., Grant, J.R., Maciejewski, A., and Wishart, D.S.
666 (2016). Heatmapper: web-enabled heat mapping for all. *Nucleic Acids Res.* **44**, W147–
667 W153.

668 Battello, N., Zimmer, A.D., Goebel, C., Dong, X., Behrmann, I., Haan, C., Hiller, K., and
669 Wegner, A. (2016). The role of HIF-1 in oncostatin M-dependent metabolic reprogramming
670 of hepatic cells. *Cancer Metab.* **4**, 3.

671 Bhargava, P., Fitzgerald, K.C., Venkata, S.L.V., Smith, M.D., Kornberg, M.D., Mowry, E.M.,
672 Haughey, N.J., and Calabresi, P.A. (2019). Dimethyl fumarate treatment induces lipid
673 metabolism alterations that are linked to immunological changes. *Ann. Clin. Transl. Neurol.*
674 **6**, 33–45.

675 Bolger, A.M., Lohse, M., and Usadel, B. (2014). Trimmomatic: A flexible trimmer for Illumina
676 sequence data. *Bioinformatics* **30**, 2114–2120.

677 Bray, M.A., Singh, S., Han, H., Davis, C.T., Borgeson, B., Hartland, C., Kost-Alimova, M.,

678 Gustafsdottir, S.M., Gibson, C.C., and Carpenter, A.E. (2016). Cell Painting, a high-content
679 image-based assay for morphological profiling using multiplexed fluorescent dyes. *Nat.*
680 *Protoc.* 11, 1757–1774.

681 Cazanave, S., Podtelezhnikov, A., Jensen, K., Seneshaw, M., Kumar, D.P., Min, H.K.,
682 Santhekadur, P.K., Banini, B., Mauro, A.G., Oseini, A.M., et al. (2017). The Transcriptomic
683 Signature of Disease Development and Progression of Nonalcoholic Fatty Liver Disease.
684 *Sci. Rep.* 7, 17193.

685 De Chiara, F., Thomsen, K.L., Habtesion, A., Jones, H., Davies, N., Gracia-Sancho, J.,
686 Manicardi, N., Hall, A., Andreola, F., Paish, H.L., et al. (2020). Ammonia Scavenging
687 Prevents Progression of Fibrosis in Experimental Nonalcoholic Fatty Liver Disease.
688 *Hepatology* 71, 874–892.

689 Chouchani, E.T., Pell, V.R., Gaude, E., Aksentijević, D., Sundier, S.Y., Robb, E.L., Logan,
690 A., Nadtochiy, S.M., Ord, E.N.J., Smith, A.C., et al. (2014). Ischaemic accumulation of
691 succinate controls reperfusion injury through mitochondrial ROS. *Nature* 515, 431–435.

692 Collison, K.S., Maqbool, Z., Saleh, S.M., Inglis, A., Makhoul, N.J., Bakheet, R., Al-Johi, M.,
693 Al-Rabiah, R., Zaidi, M.Z., and Al-Mohanna, F.A. (2009). Effect of dietary monosodium
694 glutamate on trans fat-induced nonalcoholic fatty liver disease. *J. Lipid Res.* 50, 1521–1537.

695 Dasika, S.K., Vinnakota, K.C., and Beard, D.A. (2015). Determination of the catalytic
696 mechanism for mitochondrial malate dehydrogenase. *Biophys. J.* 108, 408–419.

697 Delaglio, F., Grzesiek, S., Vuister, G.W., Zhu, G., Pfeifer, J., and Bax, A. (1995). NMRPipe:
698 A multidimensional spectral processing system based on UNIX pipes. *J. Biomol. NMR* 6,
699 277–293.

700 Dobin, A., and Gingeras, T.R. (2015). Mapping RNA-seq Reads with STAR. *Curr. Protoc.*
701 *Bioinforma.* 51, 11.14.1-11.14.19.

702 Egnatchik, R.A., Leamy, A.K., Sacco, S.A., Cheah, Y.E., Shiota, M., and Young, J.D. (2019).
703 Glutamate– oxaloacetate transaminase activity promotes palmitate lipotoxicity in rat
704 hepatocytes by enhancing anaplerosis and citric acid cycle flux. *J. Biol. Chem.* 294, 3081–
705 3090.

706 Fletcher, J.A., Deja, S., Satapati, S., Fu, X., Burgess, S.C., and Browning, J.D. (2019).
707 Impaired ketogenesis and increased acetyl-CoA oxidation promote hyperglycemia in human
708 fatty liver. *JCI Insight* 4.

709 Godoy, P., Widera, A., Schmidt-Heck, W., Campos, G., Meyer, C., Cadenas, C., Reif, R.,
710 Stöber, R., Hammad, S., Pütter, L., et al. (2016). Gene network activity in cultivated primary
711 hepatocytes is highly similar to diseased mammalian liver tissue. *Arch. Toxicol.* 90, 2513–
712 2529.

713 Han, J., He, Y., Zhao, H., and Xu, X. (2019). Hypoxia inducible factor-1 promotes liver
714 fibrosis in nonalcoholic fatty liver disease by activating PTEN/p65 signaling pathway. *J. Cell.*
715 *Biochem.* 120, 14735–14744.

716 Hardwick, R.N., Ferreira, D.W., More, V.R., Lake, A.D., Lu, Z., Manautou, J.E., Slitt, A.L.,
717 and Cherrington, N.J. (2013). Altered UDP-glucuronosyltransferase and sulfotransferase
718 expression and function during progressive stages of human nonalcoholic fatty liver
719 diseases. *Drug Metab. Dispos.* 41, 554–561.

720 Hausinger, R.P. (2004). Fe(II)/ α -ketoglutarate-dependent hydroxylases and related
721 enzymes. *Crit. Rev. Biochem. Mol. Biol.* 39, 21–68.

722 Heinz, S., Benner, C., Spann, N., Bertolino, E., Lin, Y.C., Laslo, P., Cheng, J.X., Murre, C.,
723 Singh, H., and Glass, C.K. (2010). Simple Combinations of Lineage-Determining
724 Transcription Factors Prime cis-Regulatory Elements Required for Macrophage and B Cell
725 Identities. *Mol. Cell* 38, 576–589.

726 Hiller, K., Hangebrauk, J., Jäger, C., Spura, J., Schreiber, K., and Schomburg, D. (2009).
727 Metabolite detector: Comprehensive analysis tool for targeted and nontargeted GC/MS
728 based metabolome analysis. *Anal. Chem.* 81, 3429–3439.

729 Hollinshead, K.E.R., Munford, H., Eales, K.L., Bardella, C., Li, C., Escribano-Gonzalez, C.,
730 Thakker, A., Nonnenmacher, Y., Kluckova, K., Jeeves, M., et al. (2018). Oncogenic IDH1
731 Mutations Promote Enhanced Proline Synthesis through PYCR1 to Support the
732 Maintenance of Mitochondrial Redox Homeostasis. *Cell Rep.* 22, 3107–3114.

733 Hu, H., Shu, M., He, L., Yu, X., Liu, X., Lu, Y., Chen, Y., Miao, X., and Chen, X. (2017).

734 Epigenomic landscape of 5-hydroxymethylcytosine reveals its transcriptional regulation of
735 lncRNAs in colorectal cancer. *Br. J. Cancer* **116**, 658–668.

736 Huang, D.W., Sherman, B.T., and Lempicki, R.A. (2009a). Bioinformatics enrichment tools:
737 Paths toward the comprehensive functional analysis of large gene lists. *Nucleic Acids Res.*
738 **37**, 1–13.

739 Huang, D.W., Sherman, B.T., and Lempicki, R.A. (2009b). Systematic and integrative
740 analysis of large gene lists using DAVID bioinformatics resources. *Nat. Protoc.* **4**, 44–57.

741 Huang, H., Taraboletti, A., and Shriver, L.P. (2015). Dimethyl fumarate modulates
742 antioxidant and lipid metabolism in oligodendrocytes. *Redox Biol.* **5**, 169–175.

743 Hui, S., Ghergurovich, J.M., Morscher, R.J., Jang, C., Teng, X., Lu, W., Esparza, L.A., Reya,
744 T., Zhan, L., Yanxiang Guo, J., et al. (2017). Glucose feeds the TCA cycle via circulating
745 lactate. *Nature* **551**, 115–118.

746 Kanehisa, M. (2019). Toward understanding the origin and evolution of cellular organisms.
747 *Protein Sci.* **28**, 1947–1951.

748 Kanehisa, M., and Goto, S. (2000). KEGG: Kyoto Encyclopedia of Genes and Genomes.
749 *Nucleic Acids Res.* **28**, 27–30.

750 Kanehisa, M., Sato, Y., Furumichi, M., Morishima, K., and Tanabe, M. (2019). New approach
751 for understanding genome variations in KEGG. *Nucleic Acids Res.* **47**, D590–D595.

752 Kazimierczuk, K., and Orekhov, V.Y. (2011). Accelerated NMR spectroscopy by using
753 compressed sensing. *Angew. Chemie - Int. Ed.* **50**, 5556–5559.

754 Kim, J.H., Jung, D.Y., Nagappan, A., and Jung, M.H. (2018). Histone H3K9 demethylase
755 JMJD2B induces hepatic steatosis through upregulation of PPAR γ 2. *Sci. Rep.* **8**.

756 Knobeloch, D., Ehnert, S., Schyschka, L., Büchler, P., Schoenberg, M., Kleeff, J., Thasler,
757 W.E., Nussler, N.C., Godoy, P., Hengstler, J., et al. (2012). Human hepatocytes: Isolation,
758 culture, and quality procedures. *Methods Mol. Biol.* **806**, 99–120.

759 Koliaki, C., Szendroedi, J., Kaul, K., Jelenik, T., Nowotny, P., Jankowiak, F., Herder, C.,
760 Carstensen, M., Krausch, M., Knoefel, W.T., et al. (2015). Adaptation of hepatic
761 mitochondrial function in humans with non-alcoholic fatty liver is lost in steatohepatitis. *Cell*

762 Metab. 21, 739–746.

763 Kolwankar, D., Vuppalanchi, R., Ethell, B., Jones, D.R., Wrighton, S.A., Hall, S.D., and

764 Chalasani, N. (2007). Association Between Nonalcoholic Hepatic Steatosis and Hepatic

765 Cytochrome P-450 3A Activity. Clin. Gastroenterol. Hepatol. 5, 388–393.

766 Lardy, H.A., Paetkau, V., and Walter, P. (1965). Paths of carbon in gluconeogenesis and

767 lipogenesis: the role of mitochondria in supplying precursors of phosphoenolpyruvate. Proc.

768 Natl. Acad. Sci. U. S. A. 53, 1410–1415.

769 Laukka, T., Mariani, C.J., Ihantola, T., Cao, J.Z., Hokkanen, J., Kaelin, W.G., Godley, L.A.,

770 and Koivunen, P. (2016). Fumarate and succinate regulate expression of hypoxia-inducible

771 genes via TET enzymes. J. Biol. Chem. 291, 4256–4265.

772 Laursen, T.L., Hagemann, C.A., Wei, C., Kazankov, K., Thomsen, K.L., Knop, F.K., and

773 Grønbæk, H. (2019). Bariatric surgery in patients with non-alcoholic fatty liver disease -

774 From pathophysiology to clinical effects. World J. Hepatol. 11, 138–249.

775 Liu, H., Pathak, P., Boehme, S., and Chiang, J.Y.L. (2016). Cholesterol 7 α -hydroxylase

776 protects the liver from inflammation and fibrosis by maintaining cholesterol homeostasis. J.

777 Lipid Res. 57, 1831–1844.

778 Love, M.I., Huber, W., and Anders, S. (2014). Moderated estimation of fold change and

779 dispersion for RNA-seq data with DESeq2. Genome Biol. 15, 550.

780 Ludwig, C., and Günther, U.L. (2011). MetaboLab - advanced NMR data processing and

781 analysis for metabolomics. BMC Bioinformatics 12, 366.

782 Lyall, M.J., Cartier, J., Thomson, J.P., Cameron, K., Meseguer-Ripolles, J., O'Duibhir, E.,

783 Szkolnicka, D., Villarin, B.L., Wang, Y., Blanco, G.R., et al. (2018). Modelling non-alcoholic

784 fatty liver disease in human hepatocyte-like cells. Philos. Trans. R. Soc. B Biol. Sci. 373,

785 20170362.

786 Lyall, M.J., Thomson, J.P., Cartier, J., Ottaviano, R., Kendall, T.J., Meehan, R.R., and

787 Drake, A.J. (2020). Non-alcoholic fatty liver disease (NAFLD) is associated with dynamic

788 changes in DNA hydroxymethylation. Epigenetics 15, 61–71.

789 Lynn, R., and Guynn, R.W. (1978). Equilibrium constants under physiological conditions for

790 the reactions of succinyl coenzyme A synthetase and the hydrolysis of succinyl coenzyme A
791 to coenzyme A and succinate. *J. Biol. Chem.* 253, 2546–2553.

792 McDonough, M.A., Loenarz, C., Chowdhury, R., Clifton, I.J., and Schofield, C.J. (2010).
793 Structural studies on human 2-oxoglutarate dependent oxygenases. *Curr. Opin. Struct. Biol.*
794 20, 659–672.

795 Nikolaou, N., Gathercole, L.L., Marchand, L., Althari, S., Dempster, N.J., Green, C.J., van de
796 Bunt, M., McNeil, C., Arvaniti, A., Hughes, B.A., et al. (2019). AKR1D1 is a novel regulator of
797 metabolic phenotype in human hepatocytes and is dysregulated in non-alcoholic fatty liver
798 disease. *Metabolism.* 99, 67–80.

799 Orekhov, V.Y., and Jaravine, V.A. (2011). Analysis of non-uniformly sampled spectra with
800 multi-dimensional decomposition. *Prog. Nucl. Magn. Reson. Spectrosc.* 59, 271–292.

801 Parafati, M., Kirby, R.J., Khorasanizadeh, S., Rastinejad, F., and Malany, S. (2018). A
802 nonalcoholic fatty liver disease model in human induced pluripotent stem cell-derived
803 hepatocytes, created by endoplasmic reticulum stress-induced steatosis. *DMM Dis. Model.*
804 *Mech.* 11.

805 Pollard, P.J., Loenarz, C., Mole, D.R., McDonough, M.A., Gleadle, J.M., Schofield, C.J., and
806 Ratcliffe, P.J. (2008). Regulation of Jumonji-domain-containing histone demethylases by
807 hypoxia-inducible factor (HIF)-1 α . *Biochem. J.* 416, 387–394.

808 Porcelli, A.M., Ghelli, A., Ceccarelli, C., Lang, M., Cenacchi, G., Capristo, M., Pennisi, L.F.,
809 Morra, I., Ciccarelli, E., Melcarne, A., et al. (2010). The genetic and metabolic signature of
810 oncocytic transformation implicates HIF1 α destabilization. *Hum. Mol. Genet.* 19, 1019–1032.

811 Ramírez, F., Dündar, F., Diehl, S., Grüning, B.A., and Manke, T. (2014). DeepTools: A
812 flexible platform for exploring deep-sequencing data. *Nucleic Acids Res.* 42, W187-91.

813 Rauckhorst, A.J., Gray, L.R., Sheldon, R.D., Fu, X., Pewa, A.D., Feddersen, C.R., Dupuy,
814 A.J., Gibson-Corley, K.N., Cox, J.E., Burgess, S.C., et al. (2017). The mitochondrial
815 pyruvate carrier mediates high fat diet-induced increases in hepatic TCA cycle capacity. *Mol.*
816 *Metab.* 6, 1468–1479.

817 Rector, R.S., Thyfault, J.P., Uptergrove, G.M., Morris, E.M., Naples, S.P., Borengasser, S.J.,

818 Mikus, C.R., Laye, M.J., Laughlin, M.H., Booth, F.W., et al. (2010). Mitochondrial dysfunction
819 precedes insulin resistance and hepatic steatosis and contributes to the natural history of
820 non-alcoholic fatty liver disease in an obese rodent model. *J. Hepatol.* **52**, 727–736.

821 Revill, K., Wang, T., Lachenmayer, A., Kojima, K., Harrington, A., Li, J., Hoshida, Y., Llovet,
822 J.M., and Powers, S. (2013). Genome-wide methylation analysis and epigenetic unmasking
823 identify tumor suppressor genes in hepatocellular carcinoma. *Gastroenterology* **145**, 1424–
824 35.e1–25.

825 Roach, P.L., Clifton, I.J., Fülöp, V., Harlos, K., Barton, G.J., Hajdu, J., Andersson, I.,
826 Schofield, C.J., and Baldwin, J.E. (1995). Crystal structure of isopenicillin N synthase is the
827 first from a new structural family of enzymes. *Nature* **375**, 700–704.

828 Satapati, S., Sunny, N.E., Kucejova, B., Fu, X., He, T.T., Méndez-Lucas, A., Shelton, J.M.,
829 Perales, J.C., Browning, J.D., and Burgess, S.C. (2012). Elevated TCA cycle function in the
830 pathology of diet-induced hepatic insulin resistance and fatty liver. *J. Lipid Res.* **53**, 1080–
831 1092.

832 Satapati, S., Kucejova, B., Duarte, J.A.G., Fletcher, J.A., Reynolds, L., Sunny, N.E., He, T.,
833 Arya Nair, L., Livingston, K., Fu, X., et al. (2015). Mitochondrial metabolism mediates
834 oxidative stress and inflammation in fatty liver. *J. Clin. Invest.* **125**, 4447–4462.

835 Scaini, G., Simon, K.R., Tonin, A.M., Busanello, E.N.B., Moura, A.P., Ferreira, G.C., Wajner,
836 M., Streck, E.L., and Schuck, P.F. (2012). Toxicity of octanoate and decanoate in rat
837 peripheral tissues: evidence of bioenergetic dysfunction and oxidative damage induction in
838 liver and skeletal muscle. *Mol. Cell. Biochem.* **361**, 329–335.

839 Schiöth, H.B., Boström, A., Murphy, S.K., Erhart, W., Hampe, J., Moylan, C., and Mwinyi, J.
840 (2016). A targeted analysis reveals relevant shifts in the methylation and transcription of
841 genes responsible for bile acid homeostasis and drug metabolism in non-alcoholic fatty liver
842 disease. *BMC Genomics* **17**, 462.

843 Sinton, M., Ripples, J.M., Villarin, B.L., Lyall, M., Carter, R., Morton, N., Hay, D., and Drake,
844 A. (2020). Nonalcoholic fatty liver disease is associated with decreased hepatocyte
845 mitochondrial respiration, but not mitochondrial number. *BioRxiv* 2020.03.10.985200.

846 Smith, S.A., Levante, T.O., Meier, B.H., and Ernst, R.R. (1994). Computer Simulations in
847 Magnetic Resonance. An Object-Oriented Programming Approach. *J. Magn. Reson. Ser. A*
848 *106*, 75–105.

849 Stark, R., and Brown, G. Differential Binding Analysis of ChIP-Seq Peak Data.

850 Sunny, N.E., Parks, E.J., Browning, J.D., and Burgess, S.C. (2011). Excessive hepatic
851 mitochondrial TCA cycle and gluconeogenesis in humans with nonalcoholic fatty liver
852 disease. *Cell Metab.* *14*, 804–810.

853 Suppli, M.P., Rigbolt, K.T.G., Veidal, S.S., Heebøl, S., Lykke Eriksen, P., Demant, M.,
854 Bagger, J.I., Nielsen, J.C., Oró, D., Thrane, S.W., et al. (2019). Hepatic transcriptome
855 signatures in patients with varying degrees of non-alcoholic fatty liver disease compared to
856 healthy normal-weight individuals. *Am. J. Physiol. Gastrointest. Liver Physiol.* *316*, G462–
857 G472.

858 Tahiliani, M., Koh, K.P., Shen, Y., Pastor, W.A., Bandukwala, H., Brudno, Y., Agarwal, S.,
859 Iyer, L.M., Liu, D.R., Aravind, L., et al. (2009). Conversion of 5-methylcytosine to 5-
860 hydroxymethylcytosine in mammalian DNA by MLL partner TET1. *Science* (80-.). *324*, 930–
861 935.

862 Thomson, J.P., Fawkes, A., Ottaviano, R., Hunter, J.M., Shukla, R., Mjoseng, H.K., Clark,
863 R., Coutts, A., Murphy, L., and Meehan, R.R. (2015). DNA immunoprecipitation
864 semiconductor sequencing (DIP-SC-seq) as a rapid method to generate genome wide
865 epigenetic signatures. *Sci. Rep.* *5*, 9778.

866 Thomson, J.P., Ottaviano, R., Unterberger, E.B., Lempainen, H., Muller, A., Terranova, R.,
867 Illingworth, R.S., Webb, S., Kerr, A.R.W., Lyall, M.J., et al. (2016). Loss of tet1-associated 5-
868 hydroxymethylcytosine is concomitant with aberrant promoter hypermethylation in liver
869 cancer. *Cancer Res.* *76*, 3097–3108.

870 Tyrakis, P.A., Yurkovich, M.E., Sciacovelli, M., Papachristou, E.K., Bridges, H.R., Gaude, E.,
871 Schreiner, A., D'Santos, C., Hirst, J., Hernandez-Fernaud, J., et al. (2017). Fumarate
872 hydratase loss causes combined respiratory chain defects. *Cell Rep.* *21*, 1036–1047.

873 Valenti, L., Bugianesi, E., Pajvani, U., and Targher, G. (2016). Nonalcoholic fatty liver

874 disease: cause or consequence of type 2 diabetes? *Liver Int.* 36, 1563–1579.

875 Wang, L., and Yu, S. (2016). Pathology of non-alcoholic fatty liver disease. *Int. J. Dig. Dis.* 2.

876 Wang, P., Yan, Y., Yu, W., and Zhang, H. (2019a). Role of ten-eleven translocation proteins

877 and 5-hydroxymethylcytosine in hepatocellular carcinoma. *Cell Prolif.* 52.

878 Wang, Y., Alhaque, S., Cameron, K., Meseguer-Ripolles, J., Lucendo-Villarin, B., Rashidi,

879 H., and Hay, D.C. (2017). Defined and scalable generation of hepatocyte-like cells from

880 human pluripotent stem cells. *J. Vis. Exp.* e55355–e55355.

881 Wang, Y., Tatham, M.H., Schmidt-Heck, W., Swann, C., Singh-Dolt, K., Meseguer-Ripolles,

882 J., Lucendo-Villarin, B., Kunath, T., Rudd, T.R., Smith, A.J.H., et al. (2019b). Multiomics

883 Analyses of HNF4 α Protein Domain Function during Human Pluripotent Stem Cell

884 Differentiation. *IScience* 16, 206–217.

885 WHO (2006). Obesity and overweight. In WHO Media Center, pp. 1–3.

886 Wilson, C.H., and Kumar, S. (2018). Caspases in metabolic disease and their therapeutic

887 potential. *Cell Death Differ.* 25, 1010–1024.

888 Wishart, D.S., Jewison, T., Guo, A.C., Wilson, M., Knox, C., Liu, Y., Djoumbou, Y., Mandal,

889 R., Aziat, F., Dong, E., et al. (2013). HMDB 3.0-The Human Metabolome Database in 2013.

890 *Nucleic Acids Res.* 41, D801-7.

891 Wu, H., D'Alessio, A.C., Ito, S., Wang, Z., Cui, K., Zhao, K., Sun, Y.E., and Zhang, Y.

892 (2011). Genome-wide analysis of 5-hydroxymethylcytosine distribution reveals its dual

893 function in transcriptional regulation in mouse embryonic stem cells. *Genes Dev.* 25, 679–

894 684.

895 Xiao, M., Yang, H., Xu, W., Ma, S., Lin, H., Zhu, H., Liu, L., Liu, Y., Yang, C., Xu, Y., et al.

896 (2012). Inhibition of α -KG-dependent histone and DNA demethylases by fumarate and

897 succinate that are accumulated in mutations of FH and SDH tumor suppressors. *Genes Dev.*

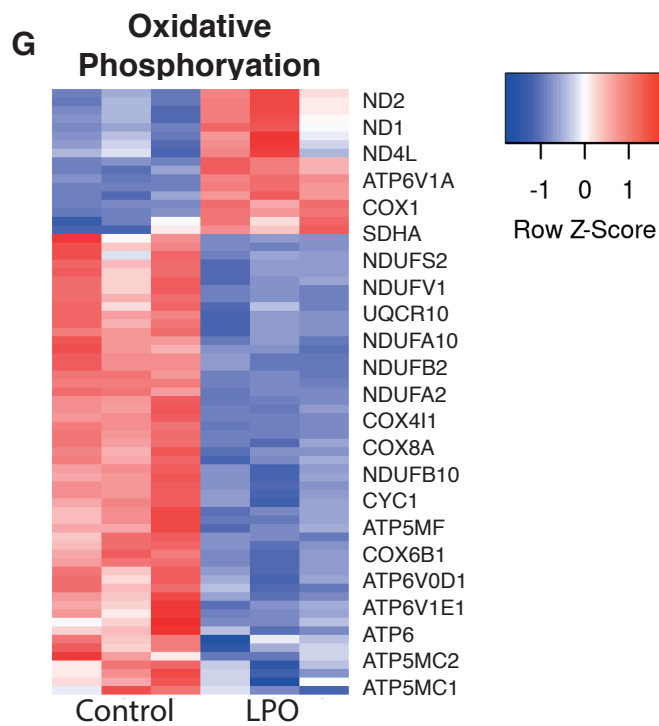
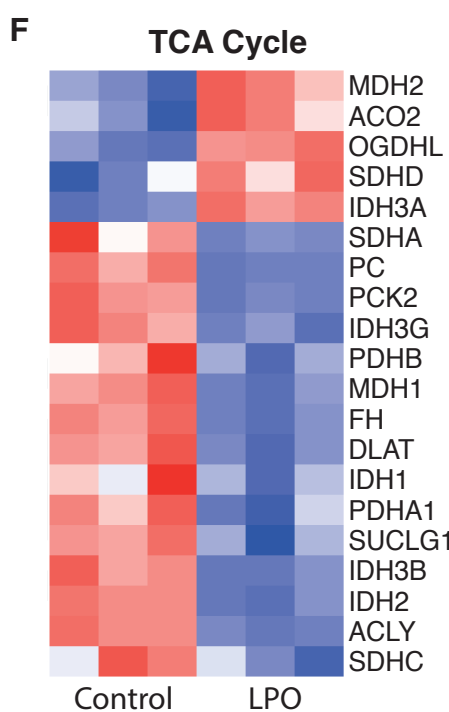
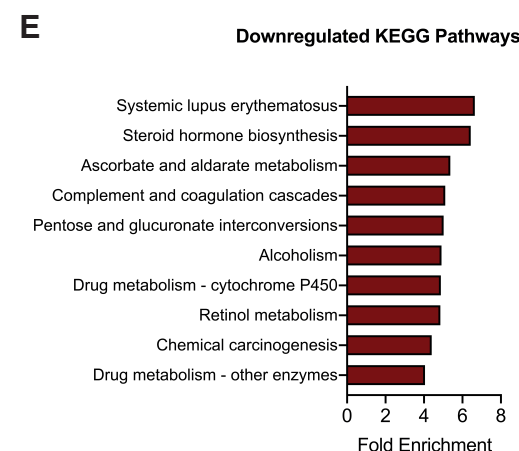
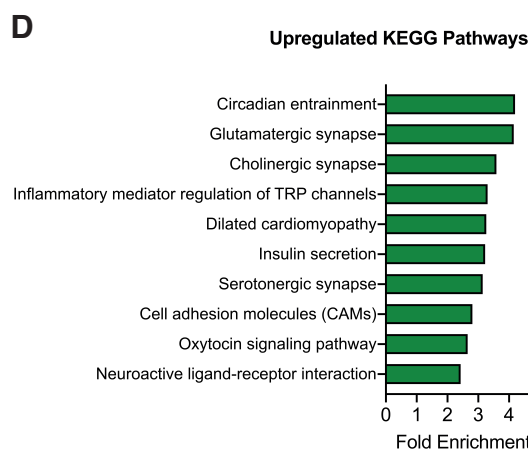
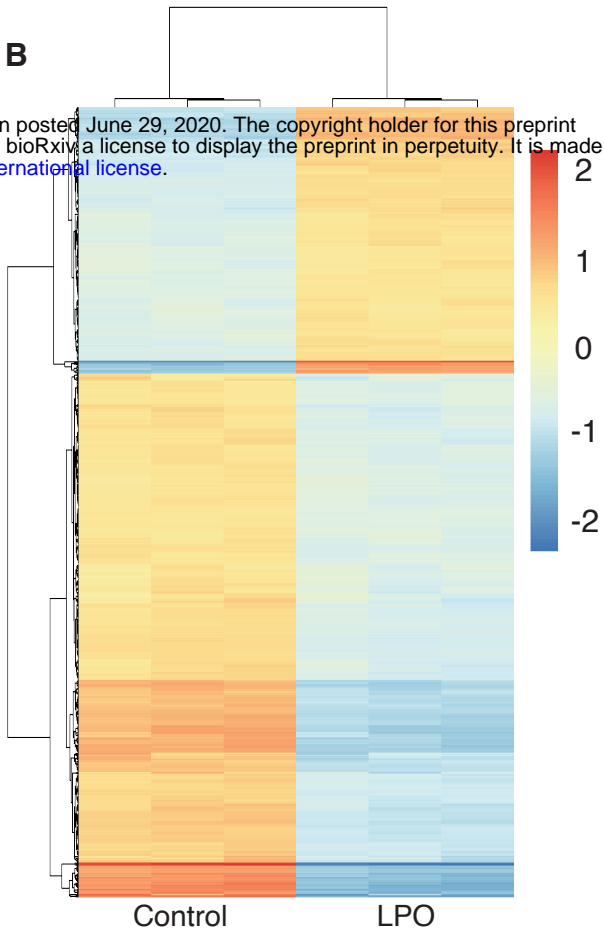
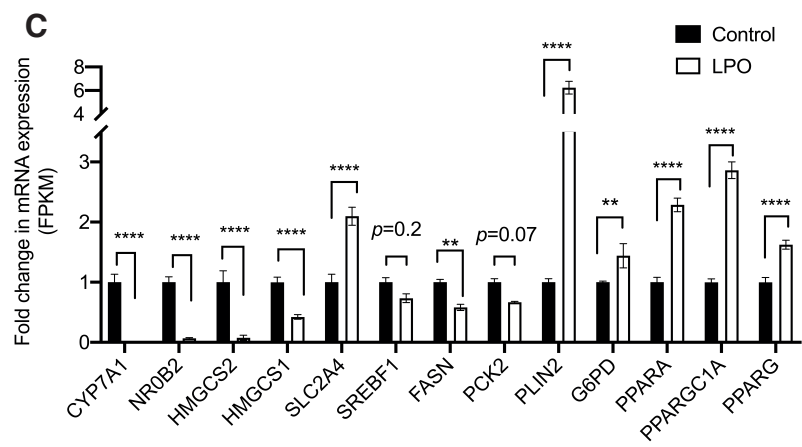
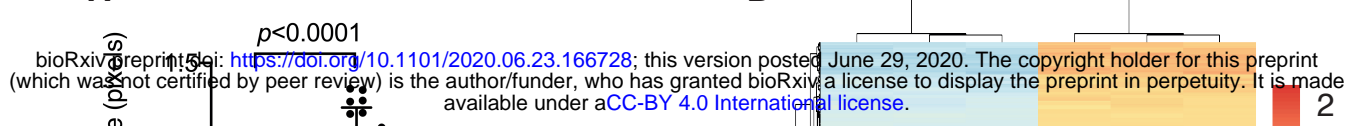
898 26, 1326–1338.

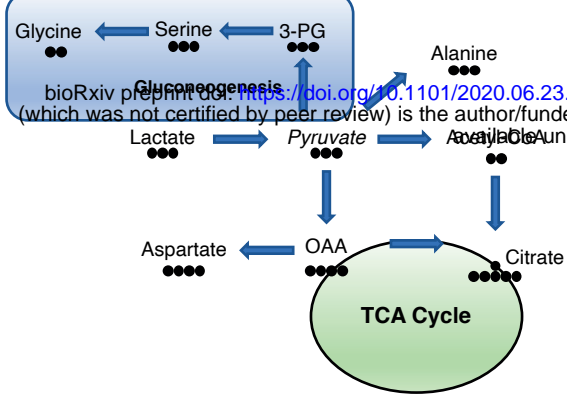
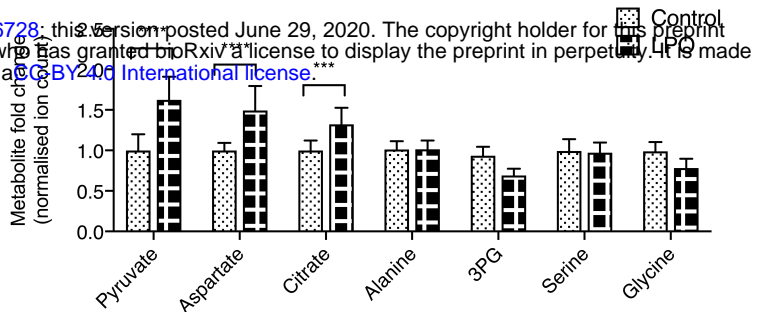
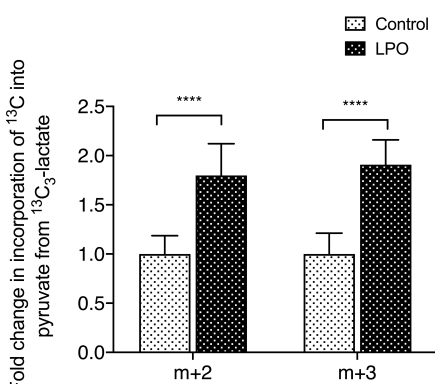
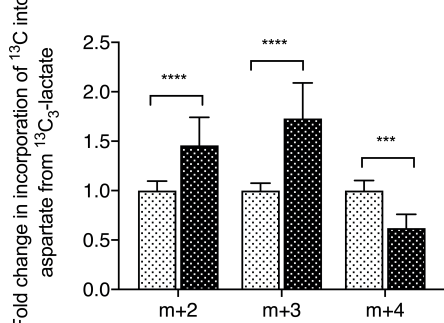
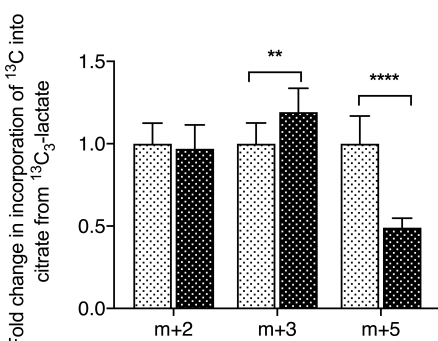
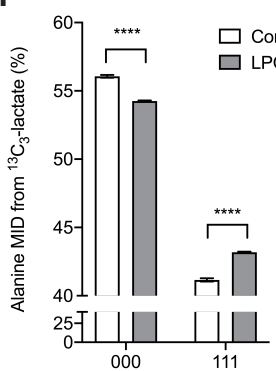
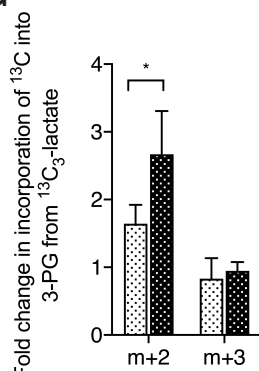
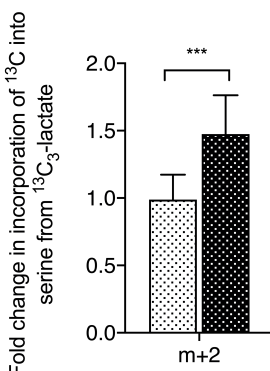
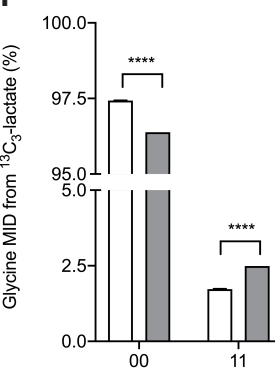
899 Yamaguchi, M., and Murata, T. (2013). Involvement of regucalcin in lipid metabolism and

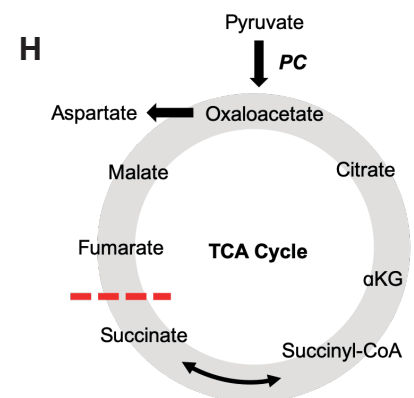
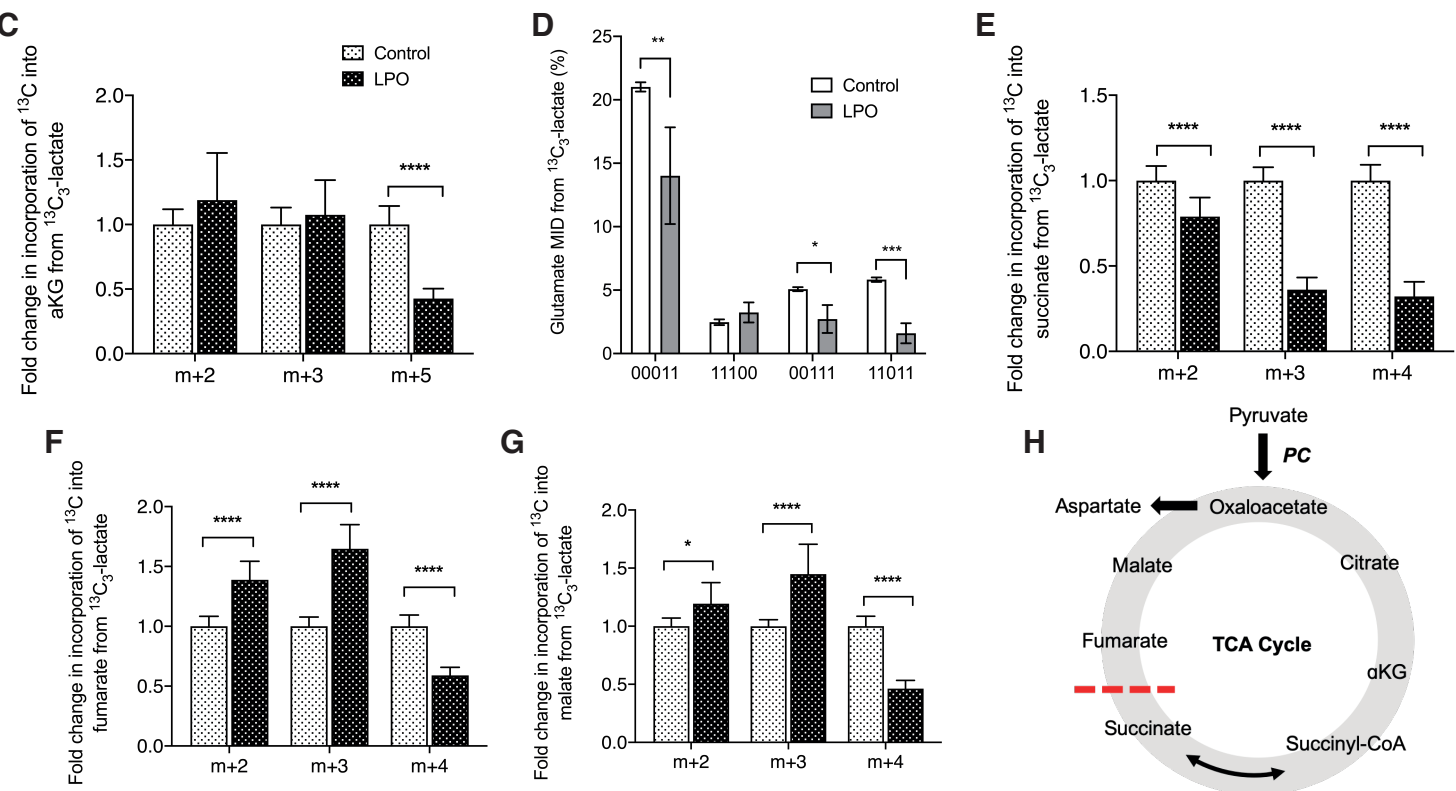
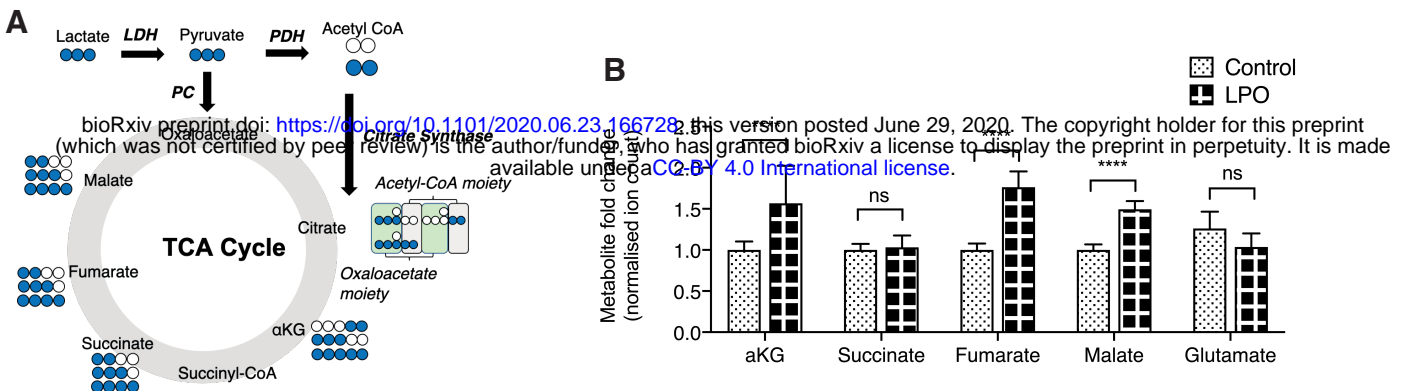
900 diabetes. *Metabolism.* 62, 1045–1051.

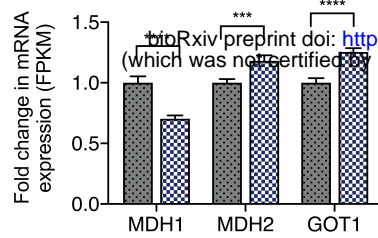
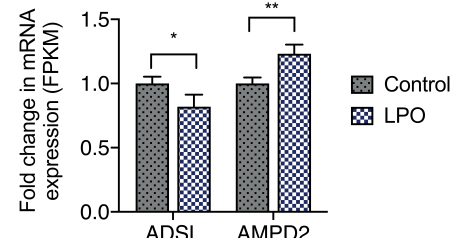
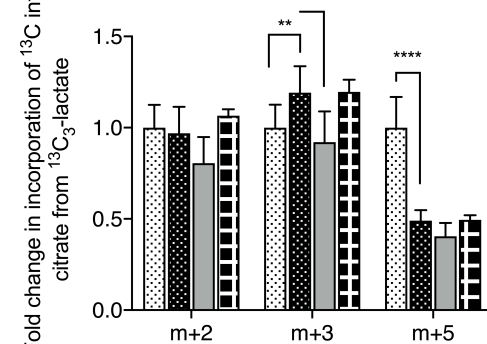
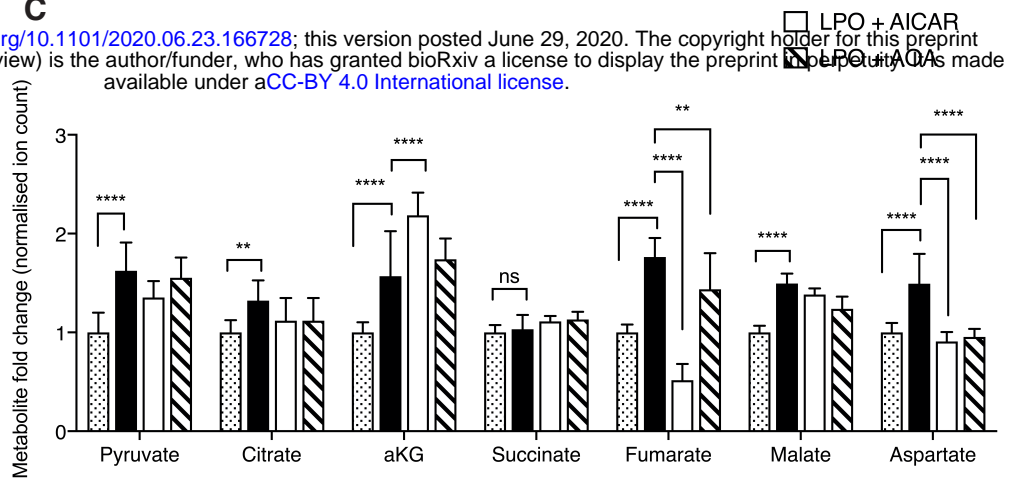
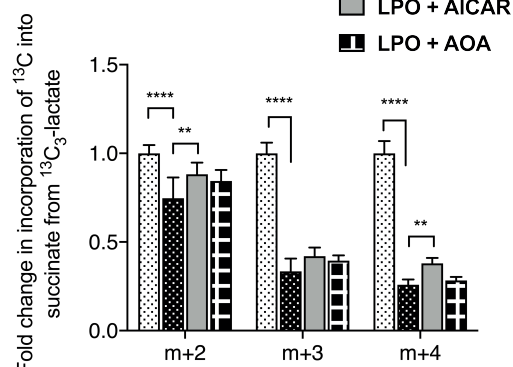
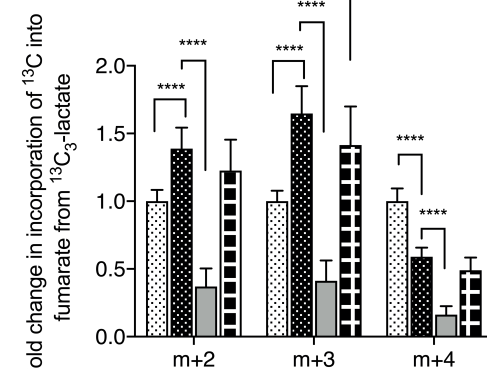
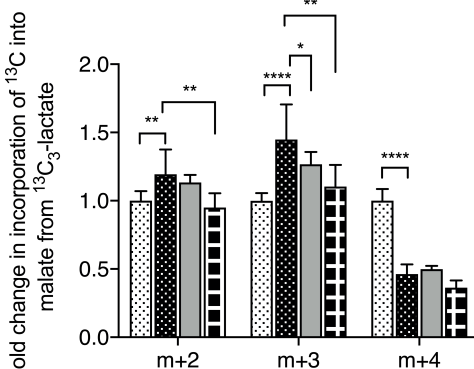
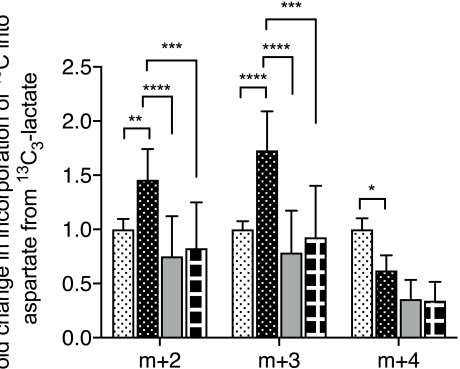
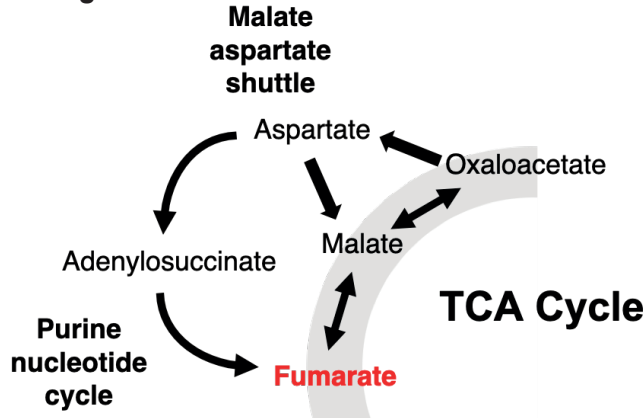
901 Zhang, Y., Liu, T., Meyer, C.A., Eeckhoute, J., Johnson, D.S., Bernstein, B.E., Nussbaum,

902 C., Myers, R.M., Brown, M., Li, W., et al. (2008). Model-based analysis of ChIP-Seq
903 (MACS). *Genome Biol.* 9, R137.
904 (2018). Picard Tools - By Broad Institute.
905



A**B****C****D****E****F****G****H****I**



A**Malate-aspartate shuttle****Purine nucleotide cycle****D****C****F****G****H****I****J****K**